Available online at www.sciencedirect.com
ScienceDirect
Journal of Power Sources 163 (2007) 784–792
JOURNAL OF POWER SOURCES
www.elsevier.com/locate/jpowsour

Effect of compression on liquid water transport and microstructure of PEMFC gas diffusion layers

A. Bazylak [a], D. Sinton [a], Z.-S. Liu [b], N. Djilali [a,*]

[a] *Department of Mechanical Engineering and the Institute for Integrated Energy Systems, University of Victoria, Victoria, BC, Canada V8W 3P6*
[b] *National Research Council, Institute for Fuel Cell Innovation, 3250 East Mall, Vancouver, BC, Canada V6T 1W5*

Received 15 July 2006; received in revised form 2 September 2006; accepted 15 September 2006
Available online 16 November 2006

Abstract

This work explores how the degradation of the gas diffusion layer (GDL) under compression contributes to the formation of preferential pathways for water transport. Fluorescence microscopy is used to provide *ex situ* visualization of liquid water transport through the GDL placed beneath an optically transparent clamping plate. Transient image data obtained with a CCD camera indicates that areas of compression in the GDL coincide with preferential pathways for water transport and break-through. Preferential flow of water through the smaller pores resulting from GDL compression is contrary to the expected behaviour in a hydrophobic medium, and this suggests a loss of hydrophobicity. Scanning electron microscopy (SEM) is used to investigate the effect of compression on the morphology of the GDL. These SEM images show that compressing the GDL causes the breakup of fibers and, indeed, deterioration of the hydrophobic coating.

Keywords: PEM fuel cell; Gas diffusion layer; Liquid water transport; Compression; Visualization

1. Introduction

Accumulation and transport of liquid water is a major factor in the operation and performance of the polymer electrolyte membrane fuel cell (PEMFC) [1]. Water is typically introduced through both anode and cathode gases to humidify the membrane and ensure good ionic conductivity. Water is also produced during the electrochemical reactions at the cathode catalyst layer. The gas diffusion layer (GDL), which supports the catalyst layer in the membrane electrode assembly of the fuel cell, is used to provide pathways for gaseous fuels to diffuse to the catalyst site and to conduct electricity from the catalyst site to the current collecting bipolar plates. Without proper water management, liquid water may accumulate in the GDL and distribution channels through condensation and reaction, causing the reactant gases traveling from the distribution channels to become restricted from reaching the catalyst sites [2]. Since water management directly affects the ionic conductivity of the PEM, the degree of catalyst flooding, and the flow in the distribution channels, improved water management will result in an increase in the power density of the PEMFC.

Fuel cells are assembled under compressive loads to prevent gas leakages, however high compressions lead to poor performance. The GDL experiences non-uniform compression because of its contact with the bipolar plate with gas flow channels. The microstructure of the GDL and consequently the dynamics of liquid water transport within may be affected by the compression. Little has been done to date to investigate such effects.

Within the last few years, there has been a major thrust to use empirical methods to analyze the water distribution in PEMFCs [3,4]. Mench et al. [3] used gas chromatography to obtain *in situ* measurements of the water vapor distribution in PEMFC gas channels. While insightful, their work does not provide information on the transport mechanisms of liquid water through the GDL. In the recent past, there have been a number of experiments in which liquid water formation and droplet movement in the channel have been visualized with the use of optically accessible flow fields and digital photography [1,5–8]. These methods [1,5] provide useful information on how flow field flooding corresponds to current density degradation, however, they do not afford the spatial

* Corresponding author. Tel.: +1 250 721 6034; fax: +1 250 721 6323.
E-mail address: ndjilali@uvic.ca (N. Djilali).

0378-7753/$ – see front matter © 2006 Elsevier B.V. All rights reserved.
doi:10.1016/j.jpowsour.2006.09.045

resolution required to analyze the transport of liquid water within the GDL, which eventually leads to channel flooding. Yang et al. [7] visualized water droplet emergence from the GDL surface and droplet growth in the gas channel, and Lu and Wang [6] observed water droplet formation on the cathode side of a direct methanol fuel cell. Recently, more advanced imaging techniques have been employed to obtain detailed information regarding liquid water formation and transport in the fuel cell, including scanning electron microscopy [9,10], nuclear magnetic resonance microscopy [11,12], neutron imaging [13–17], microtomography [18], and fluorescence microscopy [19].

Nam and Kaviany [9] employed an environmental scanning electron microscope (ESEM) to visualize condensed water droplets on GDL fibers in the absence of bulk liquid water transport. They proposed that micro-droplets agglomerate to form macro-droplets, followed by water flowing preferentially towards larger pores. The authors hypothesized that water is distributed in a branching geometry where large streams act as the backbone for macro-transport, and smaller streams transport water from micro-droplets to macro-droplets. Pasaogullari and Wang [20] also hypothesized the formation of a tree-like liquid water percolation in the GDL after condensation begins.

Feindel et al. [11] used nuclear magnetic resonance (NMR) microscopy to investigate the production and distribution of water in an operating PEMFC. Tsushima et al. [12] also recently used NMR to measure the water content distribution in the membrane of an operating PEMFC. Although these authors [11,12] were able to visualize flooding in the flow fields, the resolution of their images was not adequate to visualize the water content in the GDL.

Neutron imaging is another attractive method for visualizing water content because of the neutron's sensitivity to hydrogen atoms in water [13]. Satija et al. [13] reported the use of neutron imaging to perform *in situ* analysis of water in an operating PEMFC. Kramer et al. used neutron imaging to detect liquid accumulation in the flow field and GDL of a PEMFC [14,17] and in a DMFC [15]. Pekula et al. [16] recently reported the use of neutron imaging for the visualization of two-phase flow in an operating PEMFC. They found that at high power conditions, liquid water tended to accumulate along or under the channel walls. Radiographs showed that liquid water tended to accumulate particularly in the turns of the gas flow channels. The authors attribute this to the change in momentum of the gas flow, which results in localized pressure variations. Water accumulation in the corners may also be attributed to lower gas flow velocities. These authors [13–17] successfully used neutron imaging as a water-imaging tool for the PEMFC. They were able to provide qualitative visual evaluations of how water is transported through the flow channels, but their spatial resolution (sub-millimeter range) was inadequate to study the behaviour of liquid in the GDL prior to entering the flow channels.

Our group [19] directly visualized through-plane liquid water transport in the GDL using a fluorescent tracer. A dye solution was injected through the gas diffusion layer of a PEMFC, and fluorescence microscopy was employed to visualize the transport of liquid water through this fibrous structure. The technique allowed tracking of the time-evolving gas/liquid interfaces, and provided unique insight into the dynamics of liquid water flow through distinct pathways. Water transport was found to be dominated by fingering and channeling, rather than via a converging capillary tree suggested by prior work [9,20].

A few studies have recently examined the effects of the stack assembly pressure and the compression of the GDL on PEMFC performance [21–24]. Quantified compression pressures for the GDL in the literature are few and varied [22] due to the proprietary nature of fuel cell design as well as the difficulty in taking measurements. There is further ambiguity in quantifying the pressure applied to the GDL because the surface area in contact with the bipolar plates varies depending on the channel to land ratio.

Lee et al. [21] evaluated the performance of a PEMFC with polarization curves resulting from varying compression pressures and found that performance decreased with increasing manifolding bolt torque. A torque of 100 in. lb bolt^{-1}, corresponding to 1.61 MPa inside the fuel cell, resulted in the best performance with a Toray GDL. They suspected that higher torques damaged the GDL and decreased the electrical conductivity between the MEA and the current collecting plates, but no direct experimental evidence was provided. Recently, Escribano et al. [22] demonstrated that stress applied on an ELAT DS GDL resulted in decreased thickness and electrical conductivity. They performed two successive compressions, where the first compression (0.5 MPa) represented the pressure commonly used to make the MEAs, and the second (1.5 MPa) represented the compression caused by the current collecting plates. Lee et al. [24] performed numerical and experimental measurements of the pressure distributions inside the fuel cell with prescribed assembly stack pressures. They measured the pressure distribution between the current collecting plates and the MEA using a pressure film with assembly stack pressures of 147 through 294 MPa. An assembly stack pressure of 245 MPa was required to ensure the MEA was in full contact with the GDL and the flow field plate. This assembly stack pressure resulted in a compression of the MEA that varied between 15.2 and 46.2 MPa. Ge et al. [23] studied how GDL compression affected PEMFC performance. They achieved the best fuel cell performance with carbon fiber paper with the smallest compression ratio of 14%, which was achieved with approximately the weight of the collector plate and the end plate on top of the GDL. From these results, they concluded that an optimal compression could not be determined because a compression that is at or below this optimal value would be inadequate to seal the fuel cell. Ge et al. suggest that most fuel cells probably suffer from over-compression. These authors [21–24] focused on the effect of fuel cell performance due to varying compression pressures as well as the verification of how pressure inside the fuel cell varies spatially, however, these studies do not specifically address how liquid water transport is influenced by this pressure.

The purpose of this work is to investigate the effect of compression on liquid water transport and on the microstructure of PEMFC GDLs. The effect of GDL compression on liquid water transport is potentially very important because of the intricate relationship between pore radii and surface tension

on the transport properties of the GDL [25]. Although the fuel cell must be compressed to prevent fuel leakages, over-compressing the fuel cell results in increased fuel mass transfer resistance [22,23]. The influence of compression on water breakthrough locations in the GDL is investigated here by placing the GDL in an optically transparent clamping apparatus and using fluorescence microscopy. Transient image intensity data is correlated to the liquid surface height and used to resolve the dynamic transport of liquid water. Scanning electron microscopy is also employed to study the effects of compression on the morphology of the GDL. This work brings new insight on the influence of distribution channels on the development of GDL flooding, and documents the structural changes in the GDL due to compression.

2. Experimental

Fluorescence microscopy was utilized to visualize liquid water transport through the cross plane of a GDL. Fluorescence based visualization takes advantage of the following three-step process in which molecules that exhibit fluorescence experience the absorbance, dissipation and emission of energy [26]. The fluorescent dye employed in this work, Fluorescein (M_W 332.31), has a maximum absorbance of 490 nm (blue light) and a maximum emission wavelength of 513 nm (green light). A dilute solution (1 mM) of fluorescein was used to tag the liquid phase, as it traverses through the plane of the GDL. This dilute fluorescein dye solution (83 ppm) has negligible effects on the properties of water [27]. All wavelengths below the expected emission spectrum were filtered, and the intensity of the light detected was correlated to the height of the liquid.

2.1. Gas diffusion layer

For all of the studies reported in this paper, a Toray TGP-H-060 non-woven fibrous GDL material was used. The GDL must provide a path for product water to be removed from the catalyst layer. In order to facilitate water transport and alleviate potential flooding, the GDL is generally made hydrophobic in its bulk [25]. In practice, the GDL is commonly coated with a solution of polytetrafluoroethylene (PTFE) to increase its hydrophobicity. In particular, the GDL material studied here had a PTFE content of 10 wt.%. The Toray TGP-H-060 GDL is also a highly porous media with more than 50% of its pore sizes ranging from 30 to 40 μm [28], with a thickness of 190 μm [28], and a mean fiber diameter of 8 μm [19].

2.2. Apparatus

Fig. 1 shows the schematic of the Fluorescence Microscopy and GDL clamping apparatus. The GDL was clamped above the fluid reservoir and a compression O-ring, which compressed the GDL and prevented leakage. A plexiglas top plate with a hole in the center of diameter, $d = 2$ mm (for liquid to escape) was clamped above the GDL with eight screws. An optical microscope was used to perform the fluorescence microscopy, and images were captured with a charge-coupled device (CCD) camera (QImaging Retiga 1300i Cooled Mono 12 bits). A programmable syringe-pump (Harvard Apparatus PHD 22/2000) was used to deliver the fluorescein dye via Teflon FEP tubing (Upchurch Scientific, WA) from the syringe pump to the GDL at a rate of 0.02 ml min^{-1}. Normalized by the GDL planar area considered, and assuming no net water transport between anode and cathode, this water flow rate would correspond to high current densities [29]. The capillary number is of the order of 10^{-7}, which indicates the dominance of surface tension forces.

2.3. Data acquisition

Transient images were captured with an optical microscope (Leica Microsystems DML) with a cooled CCD camera. The results in this paper were obtained with a 1.25× magnification objective exhibiting a numerical aperture, NA, of 0.04. The theoretical depth of field is 321 μm as calculated by the

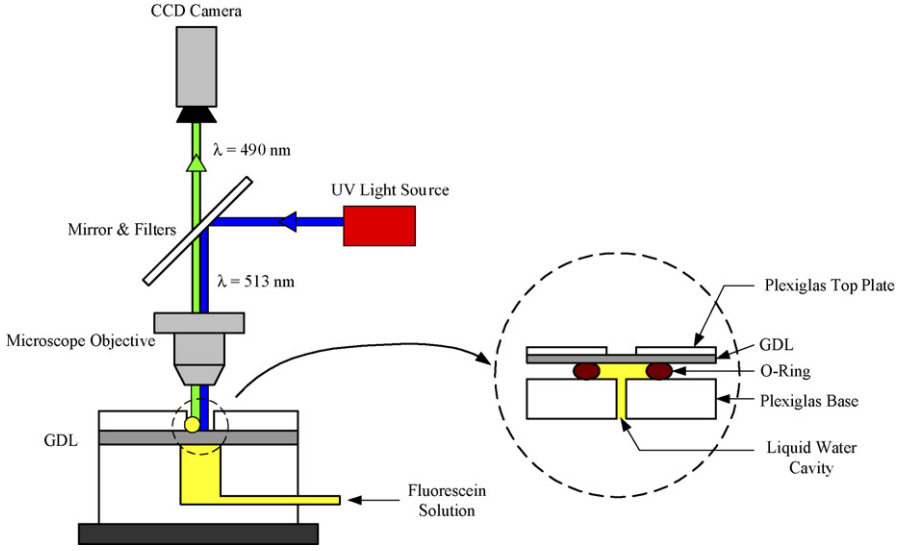

Fig. 1. Schematic of fluorescence microscopy and GDL clamping apparatus.

following expression, where λ is the wavelength of emitted light (513 nm):

$$d_{\text{field}} = \frac{\lambda}{\text{NA}^2} \quad (1)$$

The 1.25× magnification lens was used because it provided sufficient resolution of the liquid water and provided a viewing region that included the compressed regions of the GDL. Larger magnification lenses would have resulted in higher local resolution, but at the expense of a smaller viewing region. As the goal here was to ascertain the effect of compression on the GDL, a suitably large area was required to achieve a representative sample of the material. With pore sizes on the order of 30–40 μm [28], the circle defined by the compression ring's inner diameter (4 mm) corresponds to approximately 1×10^6 to 1.8×10^6 pores and is thus assumed to provide a reasonable representation of this material.

As proposed by Litster et al. [19], the fluorescence intensity field can be correlated to the through-plane height of the liquid water. The observable vertical depth presented herein is 100 μm, which is less than the theoretical depth of field because of the opacity of the GDL. The observable depth of field is supported by observations of fluorescein within the height of seven 8 μm fiber diameters and the observation of flooding above the surface of the GDL into the hole of the top plate. This depth of field results in the following eight-bit linear intensity correlation, η, where I is the eight-bit intensity data:

$$\eta = \frac{100\,\mu\text{m}}{255} I \quad (2)$$

Ideally, a high frame rate is required for a thorough analysis of the fluorescein propagation. But, since higher frame rates arrive at the cost of reduced pixel resolution, images were captured at a frame rate of 3.25 frame s^{-1}. This frame rate was achieved with a spatial resolution of 21.4 μm $pixel^{-1}$. The Hitachi S-3500N scanning electron microscope (SEM) was used to investigate the morphological changes in the GDL before and after compression of varying pressures.

2.4. Results and discussion

2.4.1. Effects of compression on liquid water transport

The GDL clamping apparatus shown in Fig. 1 was used to clamp the GDL at a prescribed pressure of 1.5 MPa, using eight screws, each with a torque of 2 in. lb. The compression pressure was calibrated using a Pressurex pressure indicating film (Sensor Products LLC, NJ). The film with a range of 0.48–2.41 MPa was inserted between the O-ring and the top clamping plate. As pressure was applied, microcapsules in the film were released providing a colour whose intensity directly relates to the amount of applied pressure. The compression pressure used here is comparable to the pressures reported by Lee et al. (1.61 MPa) [21] and Escribano et al. (0.5 and 1.5 MPa) [22].

The transport of water through the GDL, both in operating fuel cells and this experiment, is punctuated by liquid water breakthrough events which are due to liquid water pressure accumulation under the GDL. In these experiments, the location of liquid water breakthrough is of interest, rather than the behaviour of liquid water transport post breakthrough. Thus, the dye injection rate is less important than the pressure at which the dye emerged from the surface of the GDL. As the dye is injected into the bottom side of the GDL, the pressure of the dye stream increases until a critical pressure is reached. When the dye stream reaches this critical pressure, it exerts the necessary force to penetrate the GDL. Liquid water breakthrough pressure was measured with a pressure gauge (McMaster Carr) for each trial, and is listed below in Table 1. The small variations in breakthrough pressures are attributed to the non-uniform fiber orientation (and thus pore size distribution) and non-uniform PTFE coating for each particular sample used.

Table 1
Liquid breakthrough pressures

Trial #	Breakthrough pressure (kPa)
1	4.8
2	5.6
3	5.0
4	5.1
5	5.7
6	5.8
7	5.7
8	5.7
9	5.7
10	5.7

Fig. 2 shows one set of time-sequenced images of the fluorescein solution traveling through the GDL at (a) 4.9 s, (b) 5.2 s, and (c) 6.5 s. The images on the left were captured with a CCD camera projected onto the top surface of the GDL and inverted for clarity to show the evolution of water transport. The dashed concentric circles indicate where the compression O-ring is placed beneath the GDL in the clamping apparatus. To the right of each image is the three-dimensional rendering resulting from the correlation between intensity and liquid surface height. This figure shows that breakthrough occurred under the area of GDL compression, and proceeded to flood towards the center of the viewing area, where there was a hole open to atmosphere in the top clamping plate. The results shown in Fig. 2 are typical of the experimental trials conducted.

Two particular paths shown in Fig. 3 are discussed in more detail. Path 1 was the first pathway to appear during this visualization, as shown by the peak in the three-dimensional rendering in Fig. 2(a). It is also important to note that path 1 formed under the uncompressed area of the GDL, i.e. not between the concentric circles outlining the O-ring compression area. Path 2 became the dominant pathway, which formed after path 1 at 5.2 s. Although path 1 formed before path 2, path 2 became the dominant path leading to water breakthrough.

Fig. 4 shows the evolution of water surface height for paths 1 and 2. Liquid pressure accumulates under the GDL until the liquid exerts sufficient force on the GDL to traverse in the through-plane direction. At 0.92 s, path 1 rose to 6.3 μm, while path 2 had a surface height of 5.2 μm. For the next 4 s, the surface heights in paths 1 and 2 remained constant as the liquid water pressure built beneath the GDL. At 5.2 s the liquid

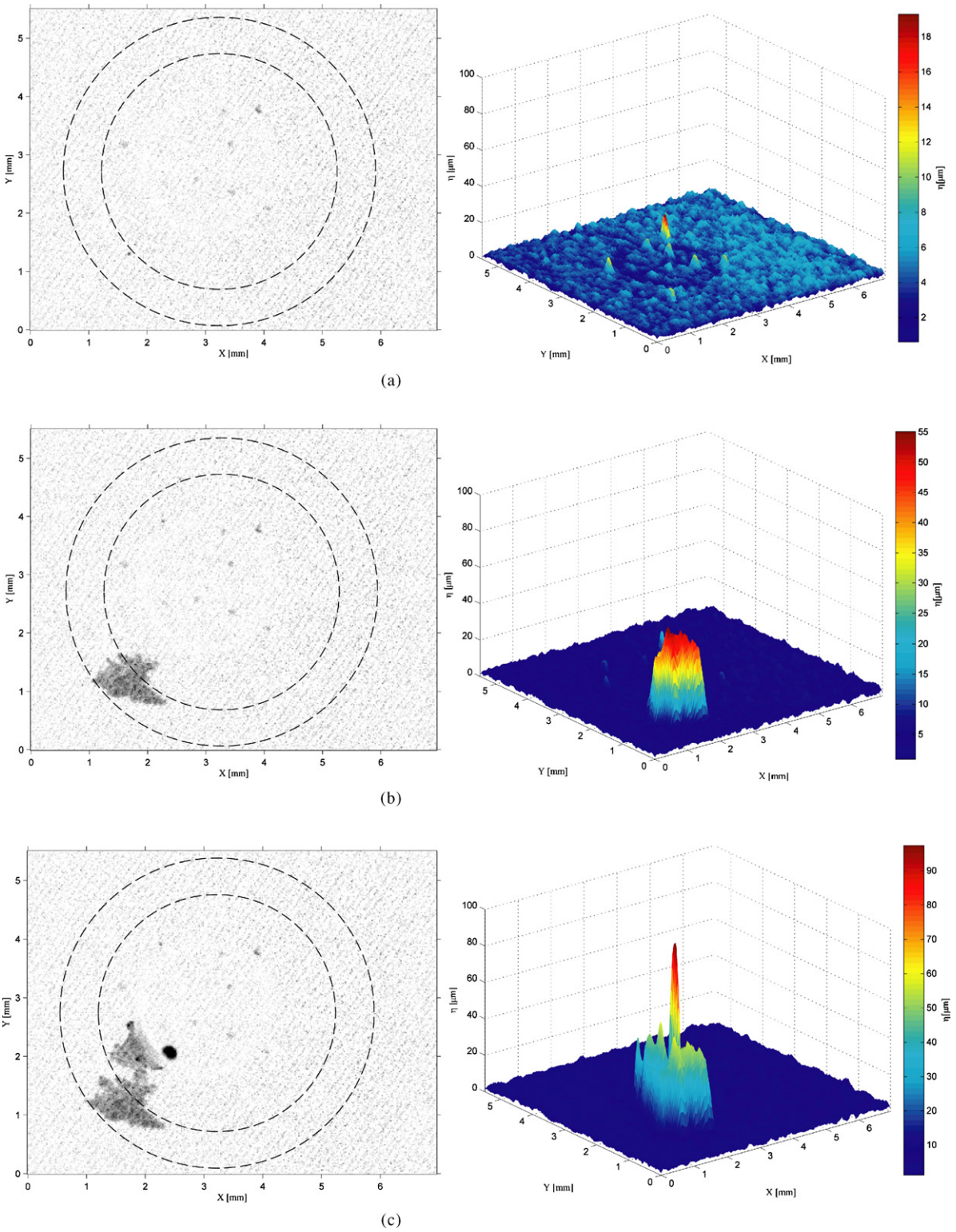

Fig. 2. Digital images from fluorescence microscopy showing the evolution of water transport at (a) $t = 4.9$ s, (b) $t = 5.2$ s, and (c) $t = 6.5$ s. Images to the left have been inverted for clarity, with the areas compressed by the O-ring shown as the area between the concentric dashed circles. To the right of each image is the three-dimensional rendering of the signal intensity.

pressure reached the critical pressure for breakthrough, and path 2 suddenly rose to a height of 55.5 μm. The liquid water pressure beneath the GDL (5.7 kPa) was sufficient to breakthrough the compressed GDL at path 2 (preferential pathway), but was insufficient to breakthrough the GDL that was not compressed (path 1).

Fig. 5 is the collection of inverted fluorescence images captured with the camera projected at the surface of the GDL

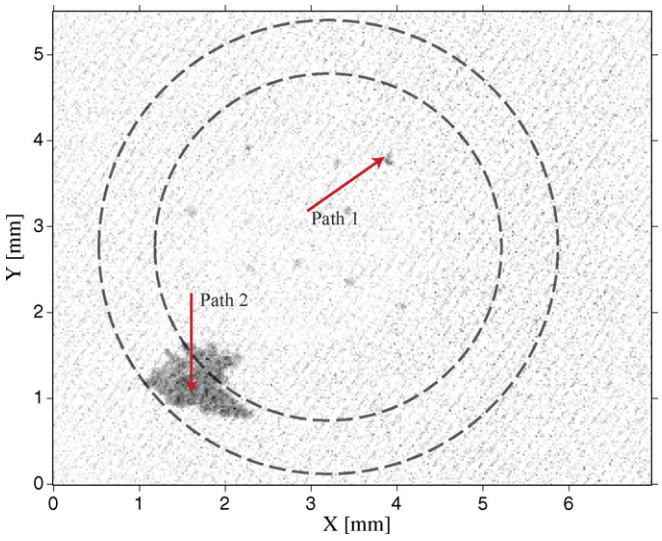

Fig. 3. Inverted fluorescence image at 5.2 s showing flow paths 1 and 2 shown in Fig. 4. The areas of the GDL that are compressed exist between the concentric dashed circles.

showing the liquid water breakthrough locations with respect to the compression O-ring for 10 trials, where trial 8 has already been discussed in detail (Figs. 2–4). As shown, all trials except for trials 3 and 5 resulted in liquid water breakthrough originating from the compressed area. The red arrows indicate where breakthrough coincided with the compression region. The blue arrows indicate where excess fluid excited through the outlet hole, post-breakthrough. If one assumes liquid water transport behaviour is the same in the compressed and uncompressed GDL, then statistically 44% of the breakthroughs should have occurred in the area defined by the compression O-ring, with a test area of 0.22 cm^2 and compression area of 0.097 cm^2, however 80% of the trials resulted in breakthroughs from the compressed area. These results indicate that areas of the GDL that are compressed are preferential pathways

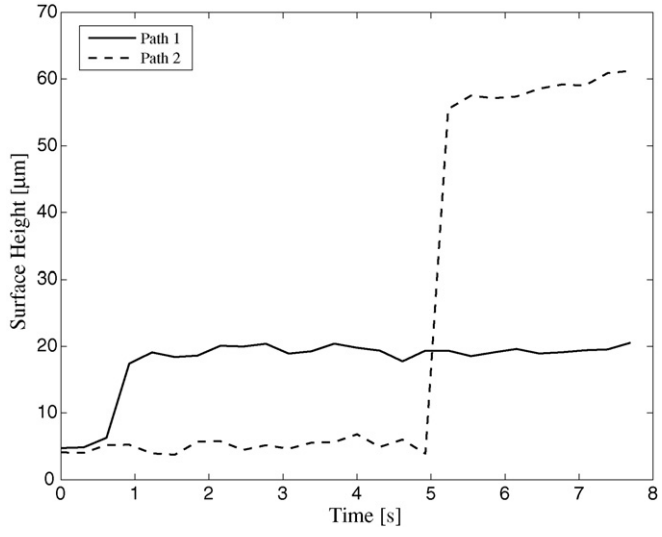

Fig. 4. The liquid water surface height determined via correlation with fluorescence intensity of paths 1 and 2, where path 1 appears in the uncompressed GDL and path 2 appears in the compressed GDL.

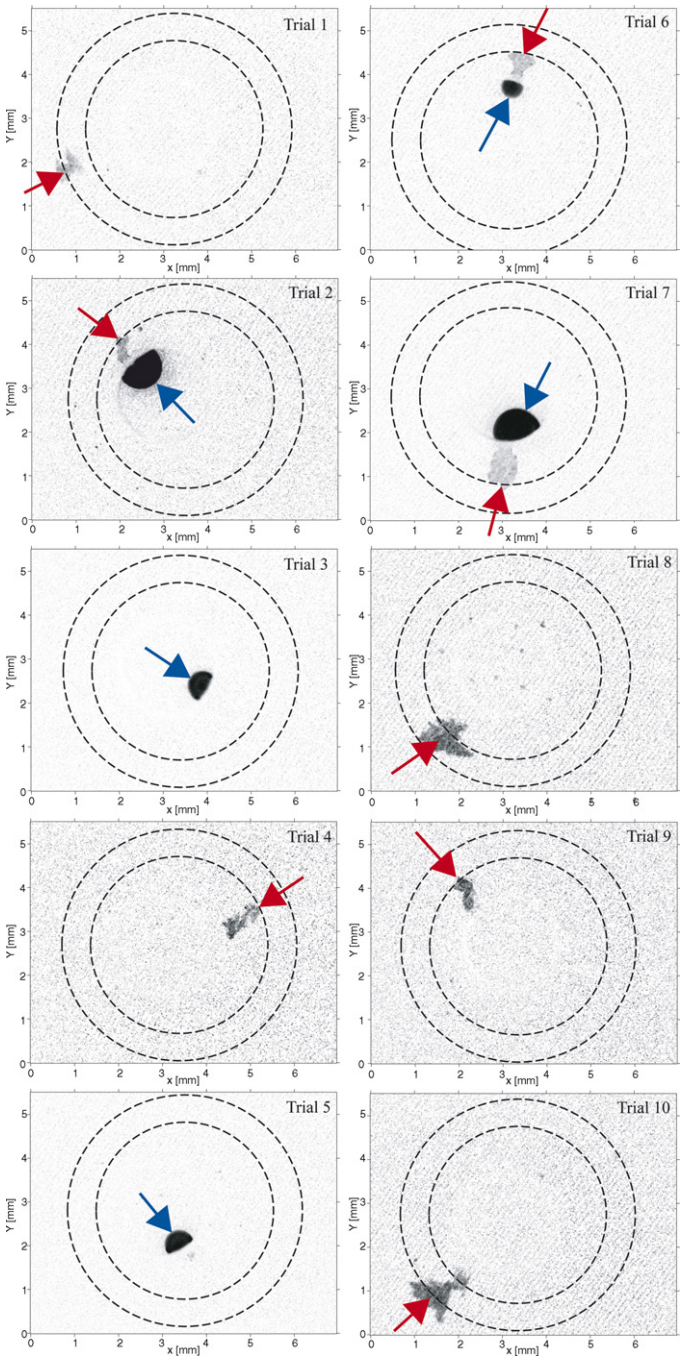

Fig. 5. Inverted fluorescence images showing the liquid water breakthrough location with respect to the compression O-ring, where all trials except for trials 3 and 5 resulted in breakthrough originating in the area above the compression O-ring. Red arrows indicate where breakthrough coincided with the compression region. The blue arrows indicate where excess fluid excited through the outlet hole, post-breakthrough. (For interpretation of the references to colour in this figure legend, the reader is referred to the web version of the article.)

for liquid water transport. These results are counter-intuitive because, in general, the compression of hydropho-bic porous media results in smaller mean pore sizes. In the absence of other effects, a decrease in hydrophobic pore size results in a marked decrease in liquid permeability [25]. Thus, it would be expected that liquid water transport through an uncompressed GDL would be favored over an otherwise similar locally compressed

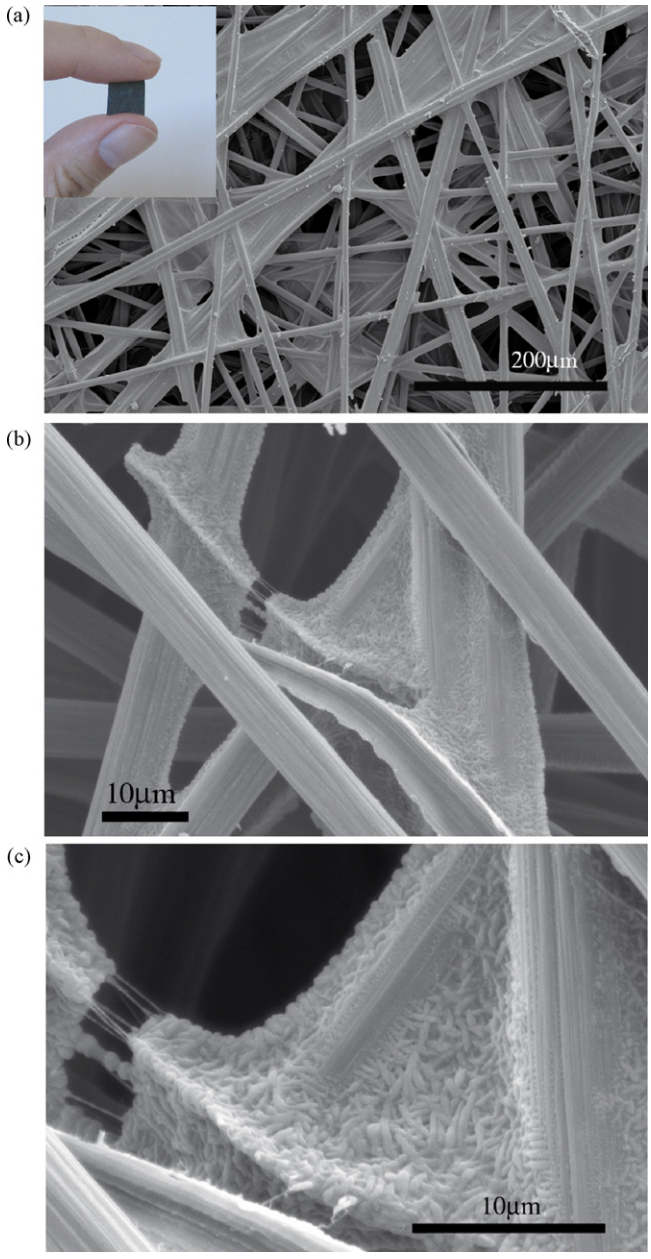

Fig. 6. SEM images of a Toray TGP-H-060 GDL with 10% PTFE treatment before compression at (a) 200× magnification with a hand-held 1 cm × 1 cm sample (inset), (b) 800× magnification, and (c) enlarged image of (b) at 4000× magnification.

GDL, whereas the opposite is observed here. These results suggest that the compression of the GDL result in additional effects that significantly influence liquid water transport in these materials. The effect of compression on the GDL morphology is investigated next.

2.4.2. Compression effects on GDL microstructure

Using the Hitachi S-3500N SEM as a conventional high-vacuum SEM, the morphological changes in the microstructure of the GDL after compression were investigated at varying pressures. Fig. 6(a) shows an SEM image of a Toray TGP-H-060 GDL at 200× magnification prior to compression, with a hand-held 1 cm × 1 cm sample (inset). This image illustrates that without compression the GDL fibers are intact. Fig. 6(b) shows the intact PTFE coating on the uncompressed GDL at 800× magnification, which is further enlarged to 4000× magnification in (c). Fig. 6(b) and (c) shows that the PTFE coating tends to accumulate on the webbing of carbonized thermoset resin, which binds the carbon fibers together. Despite the localized tendency for PTFE to accumulate in the areas where fibers intersect, the PTFE treatment of the entire GDL surface is generally continuous.

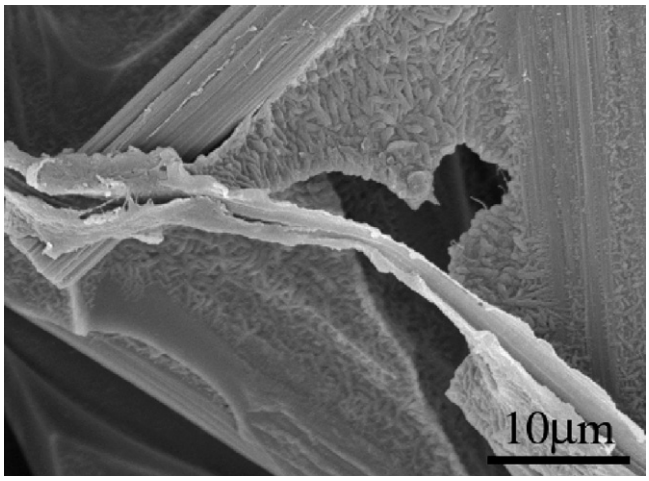

Fig. 7. SEM image of a Toray TGP-H-060 GDL with 10% PTFE treatment after it was compressed for 5 min at 0.18 MPa at 1000× magnification with a 10 kV beam voltage showing the damaged PTFE coating.

To investigate how compression affects the morphology of the GDL, the SEM was used to visualize GDL samples (0.25 cm^2) that were compressed at 0.18, 0.36, 0.68, and 1.37 MPa for 5 min. At 1000× magnification, Fig. 7 shows the breakage in the PTFE coating. Fig. 7 indicates that the breakage occurs in the 'webbing', but that also PTFE can detach from the fibers, as shown in with the upper left carbon fiber. This image also shows some PTFE coating that has been twisted and pulled midway through the left image.

Fig. 8 shows the SEM images of the GDL at 200× magnification after it was compressed for 5 min at (a) 0.18, (b) 0.36, (c) 0.68, and (d) 1.37 MPa. These images show that as the compression pressure increases, the severity and extent of the damage also increases. With a compression of 0.18 MPa, the damage to the GDL was non-uniform. This non-uniformity is attributed to the surface roughness of the GDL. As the GDL is compressed, the thickest areas of the GDL will experience damage first. However, as the compression pressure increased, the damage became more isotropic throughout the sample. The damage observed in the sample compressed at 1.37 MPa in Fig. 8(d) is characteristic of the damage to the GDLs used in the fluorescence microscopy visualizations, since they were clamped at 1.5 MPa, which is characteristic of reported pressures encountered in fuel cell studies [21,22].

The irreversible damage at the surface of the GDL has a dramatic impact on water transport behaviour, particularly at the breakthrough location. As the fibers break and PTFE coating disintegrates, the fiber edges that were not treated with PTFE

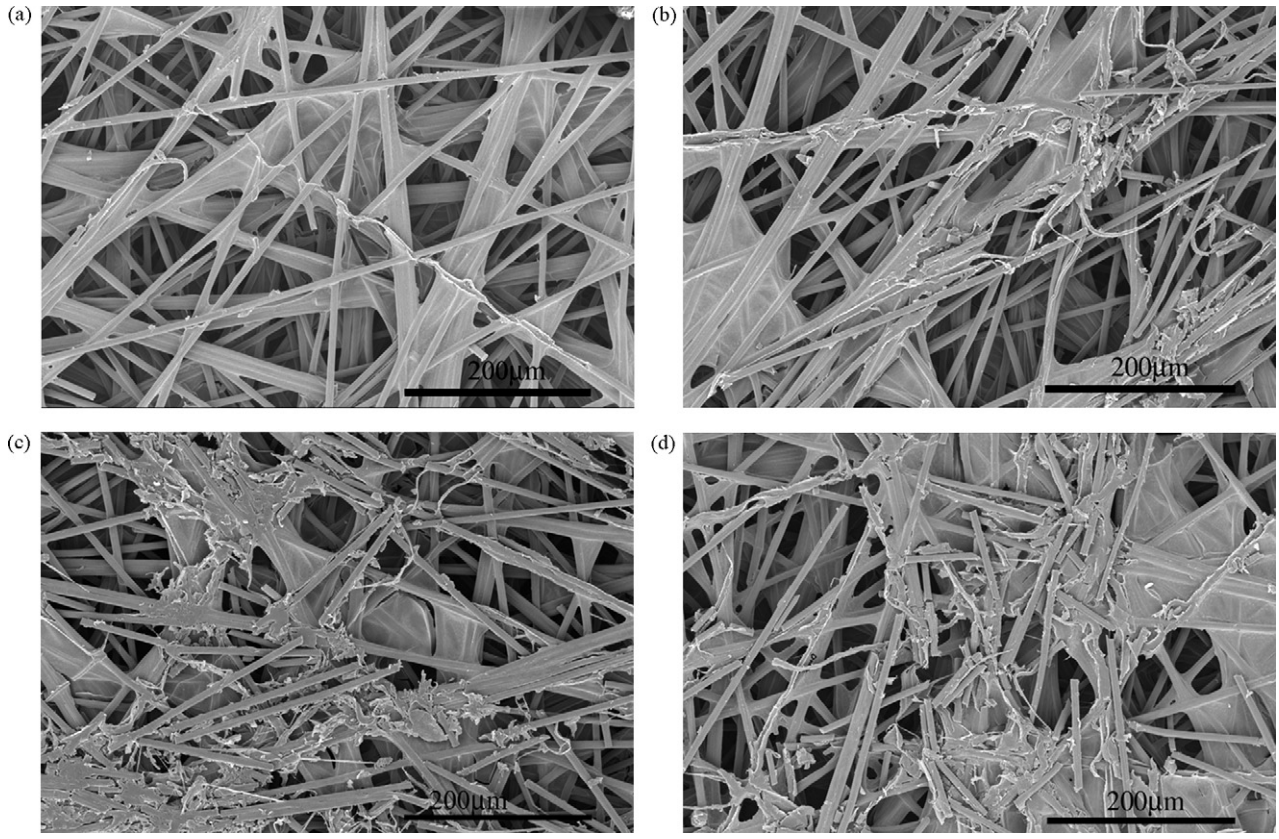

Fig. 8. SEM images of the GDL at 200x magnification after it has been compressed for five minutes at (a) 0.18 MPa, (b) 0.36 MPa, (c) 0.68 MPa, and (d) 1.37 MPa.

become exposed, locally producing a greater proportion of hydrophillic surface area. According to the sessile drop method [28], the contact angle of Toray TGP-H-060 with 9 wt.% is 156°, which is expected to be approximately the contact angle for the GDL used in this work (TGPH-060 with 10 wt.%). In contrast to the hydrophobic PTFE coated fibers, the contact angle of an untreated carbon fiber is likely to be similar to an untreated graphite plate that has a contact angle of 70–80° [7]. The localized hydrophillic pathways that were produced by fiber breakage become preferential pathways for water transport in the bulk hydrophobic GDL. Larger pores may also be created by fiber breakage, which would provide a decrease in flow resistance in the hydrophobic regions. Furthermore, multiphase flow in the GDL becomes more complex due to the mobile PTFE components that have been damaged. These detached chips of PTFE would presumably be removed from the GDL with the bulk water transport. This would, overall, reduce the hydrophobicity of the GDL compared to the original material. Pekula et al. [16] attributed their observations of the tendency for water to accumulate along channel walls and under the land area to slower gas velocities, however the work presented here suggests that the areas where the GDL is compressed become preferential pathways for liquid water transport.

3. Conclusion

Compressing a PEMFC GDL has a large influence on liquid water transport behaviour as well as on the GDL microstructure morphology. Fluorescence microscopy was applied to provide *ex situ* visualizations, showing that the compressed GDL provides preferential pathways for water transport and breakthrough. SEM images clearly illustrating the degradation of the GDL under varying compression pressures were presented. The irreversible damage at the surface of the GDL consists of fiber and PTFE coating breakage and deformation, which locally produce greater proportions of hydrophillic to hydrophobic surface area. Preferential pathways for water transport are a result of these localized hydrophillic pathways in the bulk hydrophobic GDL. The present work shows that compression alters liquid water transport and favors flow in the compressed areas of the GDL (under the land area) due to both morphological changes and possible loss of hydrophobicity. With respect to fuel cell operation, this liquid water transport behaviour may be beneficial as water can be channeled to where transport is less critical. Liquid water transport in the fuel cell could be further controlled by pre-compressing the material in strategic locations to facilitate removal of excess water in the assembled cell.

Acknowledgements

The authors are grateful for the financial support of the Natural Sciences and Engineering Research Council (NSERC) of Canada, the Canada Research Chair Program, and the National Research Council (NRC).

References

[1] K. Tiiber, D. Pcza, C. Hebling, J. Power Sources 124 (2003) 403–414.
[2] T. Berning, N. Djilali, J. Electrochem. Soc. 150 (12) (2003) A1589–A1598.
[3] M. Mench, Q. Dong, C. Wang, J. Power Sources 124 (2003) 90–98.
[4] J. Stumper, M. Lhr, S. Hamada, J. Power Sources 143 (2005) 150–157.
[5] A. Hakenjos, H. Muenter, U. Wittstadt, C. Hebling, J. Power Sources 131 (2004) 213–216.
[6] G. Lu, C. Wang, J. Power Sources 134 (2004) 33–40.
[7] X. Yang, F. Zhang, A. Lubawy, C. Wang, Electrochem. Solid-State Lett. 7 (11) (2004) A408–A411.
[8] K. Sugiura, M. Nakata, T. Yodo, Y. Nishiguchi, M. Yamauchi, Y. Itoh, J. Power Sources 145 (2005) 526–533.
[9] J. Nam, M. Kaviany, Int. J. Heat Mass Transfer 46 (2003) 4595–4611.
[10] C. Lim, C. Wang, Electrochim. Acta 49 (2004) 4149–4156.
[11] K. Feindel, L.-A. LaRocque, D. Starke, S. Bergens, R. Wasylishen, J. Am. Chem. Soc. 126 (2004) 11436–11437.
[12] S. Tsushima, K. Teranishi, K. Nishida, S. Hirai, Magn. Reson. Imaging 23 (2005) 255–258.
[13] R. Satija, D. Jacobson, M. Arif, S. Werner, J. Power Sources 129 (2004) 238–245.
[14] D. Kramer, J. Zhang, R. Shimoi, E. Lehmann, A. Wokaun, K. Shinohara, G. Scherer, Electrochim. Acta 50 (2005) 2603–2614.
[15] D. Kramer, E. Lehmann, G. Frei, P. Vontobel, A. Wokaun, G. Scherer, Nuclear Instrum. Methods Phys. Res. A 542 (2005) 52–60.
[16] N. Pekula, K. Heller, P. Chuang, A. Turhan, M. Mench, J. Brenizer, K. Unlu, Nuclear Instrum. Methods Phys. Res. A 542 (2005) 134–141.
[17] J. Zhang, D. Kramer, R. Shimoi, Y. Ono, E. Lehmann, A. Wokaun, K. Shinohara, G. Scherer, Electrochim. Acta 51 (2006) 2715–2727.
[18] P.K. Sinha, P. Halleck, C.-Y. Wang, Electrochem. Solid-State Lett. 9 (7) (2006) A244–A348.
[19] S. Litster, D. Sinton, N. Djilali, J. Power Sources 154 (2006) 95–105.
[20] U. Pasaogullari, C. Wang, J. Electrochem. Soc. 151 (3) (2004) A399–A406.
[21] W.-K. Lee, C.-H. Ho, J. Van Zee, M. Murthy, J. Power Sources 84 (1999) 45–51.
[22] S. Escribano, J.-F. Blachot, J. Etheve, A. Morin, R. Mosdale, J. Power Sources 156 (2006) 8–13.
[23] J. Ge, A. Higier, H. Liu, J. Power Sources 159 (2006) 922–927.
[24] S.-J. Lee, C.-D. Hsu, C.-H. Huang, J. Power Sources 145 (2005) 353–361.
[25] S. Litster, N. Djilali, Transport Phenomena in Fuel Cells, WIT Press, Southampton, UK, 2005, pp. 175–213.
[26] D. Sinton, Microfluid Nanofluid 1 (2004) 2–21.
[27] H. Anderson, S. Fu, T. Myers, C. Thompson, Proceedings of the 9th International Symposium on Flow Visualization, 2000, pp. 1–7 (paper 8).
[28] M. Mathias, J. Roth, J. Fleming, W. Lehnert, Handbook of Fuel Cells, John Wiley and Sons, Ltd., New York, 2003, pp. 1–21.
[29] E. Kumbur, K. Sharp, M. Mench, J. Power Sources 161 (2006) 333–345.